Cellular/Molecular

Target-Cell-Specific Left–Right Asymmetry of NMDA Receptor Content in Schaffer Collateral Synapses in ε1/NR2A Knock-Out Mice

Yue Wu,[1,2] **Ryosuke Kawakami,**[3] **Yoshiaki Shinohara,**[2] **Masahiro Fukaya,**[4] **Kenji Sakimura,**[5] **Masayoshi Mishina,**[6] **Masahiko Watanabe,**[4] **Isao Ito,**[3] **and Ryuichi Shigemoto**[1,2,7]

[1]Department of Physiology, School of Life Science, Graduate University for Advanced Studies (Sokendai), Okazaki, Aichi 444-8787, Japan, [2]Division of Cerebral Structure, National Institute for Physiological Sciences, Okazaki, Aichi 444-8787, Japan, [3]Department of Biology, Faculty of Science, Kyushu University, Fukuoka 812-8581, Japan, [4]Department of Anatomy, Hokkaido University School of Medicine, Sapporo 060-8638, Japan, [5]Department of Cellular Neurobiology, Brain Research Institute, Niigata University, Niigata 951-8585, Japan, [6]Department of Molecular Neurobiology and Pharmacology, School of Medicine, University of Tokyo, Tokyo 113-0033, Japan, and [7]Solution-Oriented Research for Science and Technology, Japan Science and Technology Agency, Kawaguchi 332-0012, Japan

Input-dependent left–right asymmetry of NMDA receptor ε2 (NR2B) subunit allocation was discovered in hippocampal Schaffer collateral (Sch) and commissural fiber pyramidal cell synapses (Kawakami et al., 2003). To investigate whether this asymmetrical ε2 allocation is also related to the types of the postsynaptic cells, we compared postembedding immunogold labeling for ε2 in left and right Sch synapses on pyramidal cells and interneurons. To facilitate the detection of ε2 density difference, we used ε1 (NR2A) knock-out (KO) mice, which have a simplified NMDA receptor subunit composition.

The labeling density for ε2 but not ζ1 (NR1) and subtype 2/3 glutamate receptor (GluR2/3) in Sch-CA1 pyramidal cell synapses was significantly different between the left and right hippocampus with opposite directions in strata oriens and radiatum; the left to right ratio of ε2 labeling density was 1:1.50 in stratum oriens and 1.44:1 in stratum radiatum. No significant difference, however, was detected in CA1 stratum radiatum between the left and right Sch-GluR4-positive (mostly parvalbumin-positive) and Sch-GluR4-negative interneuron synapses. Consistent with the anatomical asymmetry, the amplitude ratio of NMDA EPSCs to non-NMDA EPSCs in pyramidal cells was approximately two times larger in right than left stratum radiatum and vice versa in stratum oriens of ε1 KO mice. Moreover, the amplitude of long-term potentiation in the Sch-CA1 synapses of left stratum radiatum was significantly larger than that in the right corresponding synapses. These results indicate that the asymmetry of ε2 distribution is target cell specific, resulting in the left–right difference in NMDA receptor content and plasticity in Sch-CA1 pyramidal cell synapses in ε1 KO mice.

Key words: NMDA receptor; hippocampus; pyramidal cell; interneuron; asymmetry; NR2B; GluR4; NR2A; NR2D; postembedding; knock-out; LTP

Introduction

Most of the neurons in the CNS receive excitatory inputs from several sources; meanwhile, single excitatory afferent can also innervate several types of postsynaptic target cells. Hippocampal CA1 pyramidal cells and interneurons both receive the vast majority of their excitatory inputs from Schaffer collaterals (Sch) and commissural fibers arising from the ipsilateral and contralateral CA3 pyramidal cells, respectively (Ishizuka et al., 1990). The fast excitatory synaptic transmission in these inputs is mainly mediated by AMPA- and NMDA-type glutamate receptors

(GluRs). Localization of the glutamate receptors in the CA area is different depending on input pathways as well as on target cell types (Shigemoto et al., 1996; Gottmann et al., 1997; Nusser et al., 1998a; Ito et al., 2000). For example, mossy fiber synapses had approximately four times higher AMPA receptor number than associational/commissural (A/C) fiber synapses on CA3 pyramidal cells, suggesting input-pathway-dependent receptor distribution (Nusser et al., 1998a). Conversely, A/C synapses on interneurons had approximately four times higher AMPA receptor number than those on pyramidal cells, suggesting target-cell-dependent receptor distribution (Nusser et al., 1998a). The abundance of ζ1 subunit of NMDA receptor (NR) in hippocampal neurons was also cell type dependent (Nyiri et al., 2003); pyramidal cell spines had much higher density for NR1 (ζ1) than parvalbumin (PV)-positive interneuron dendrites in stratum radiatum.

Among seven known subunits of NMDA receptors, GluRζ1

(NR1), GluRε1–GluRε4 (NR2A–NR2D) and GluRχ1–GluRχ2 (NR3A–NR3B) (Nakanishi, 1992; Sucher et al., 1995; Matsuda et al., 2002). ζ1, ε1, and ε2 subunits are most strongly expressed in the CA1 area of the adult rodent hippocampus (Monyer et al., 1994; Fritschy et al., 1998; Watanabe et al., 1998). Little is known, however, about quantitative distribution of synaptic ε subunits in the hippocampus. Recently, asymmetrical ε2 subunit contribution to synaptic NMDA response was discovered in Sch-pyramidal cell synapses between the left and right hippocampus and between the apical and basal dendrites of single pyramidal cells (Kawakami et al., 2003). The ε2 subunit allocation was also suggested to be input dependent; synapses made by ipsilateral (Sch) and contralateral (commissural) fibers had distinct ε2 components of NMDA EPSPs (Kawakami et al., 2003). To further investigate whether this asymmetrical ε2 content is also related to the types of postsynaptic cells, we examined the ε2 distribution in individual synapses made by single type of input (Sch) on different postsynaptic targets, pyramidal cells, and two populations of interneurons in the CA1 area by quantitative postembedding immunogold labeling. This method has been successfully applied to compare GABA_A and ionotropic glutamate receptor contents of distinct synapse populations (Nusser et al., 1996, 1998a; Takumi et al., 1999). We show that ε2 distribution is asymmetrical between left and right Sch-pyramidal cell but not Sch-interneuron synapses, indicating a postsynaptic cell-type-dependent regulation of the asymmetry. Also, we found that, in ε1 knock-out (KO) mice, the asymmetry of ε2 allocation results in left–right difference in NMDA receptor content and synaptic plasticity.

Materials and Methods

Ventral hippocampal commissure transection. To examine synapses made by ipsilateral Sch fibers selectively, ventral hippocampal commissure (VHC) was transected 5 d before fixation and electrophysiological recording (Kawakami et al., 2003). Wild-type (WT) and ε1 KO mice (9–10 weeks, C57BL/6 genetic background) (Sakimura et al., 1995) were anesthetized by pentobarbital injection (60 mg/kg, i.p.) and held on a stereotaxic apparatus. A small piece of razor blade (2.5 mm wide) was glued onto a rod that was clamped on a micromanipulator. From an opening (3 mm wide and 4 mm long, including the bregma) made in the skull, the blade was inserted 4.0 mm vertically at the midline of the brain to transect the VHC. To avoid damaging the sagittal sinus, the blade was initially shifted 0.5 mm to the right and inserted 0.5 mm into the cerebral cortex and was then returned to the midline position as the blade was lowered. After slowly removing the blade, a piece of skull was returned to the hole, and the scalp was closed with sutures. Animals that underwent this procedure were viable for more than 3 months. For all animals used in this study, complete transection of VHC (bregma, −0.22 to −0.82 mm) was confirmed in 150-μm-thick horizontal or coronal serial slices. All experiments were performed under the guidance of Animal Experiments in Faculty of Sciences, Kyushu University and the law (number 105) and notification (number 6) of the government.

Tissue preparation for electron microscopy. Five days after the VHC transection, WT and ε1 subunit KO mice were anesthetized by pentobarbital (60 mg/kg, i.p.) and perfused with 25 mM PBS, pH 7.4, transcardially followed by fixative containing 4% paraformaldehyde, 0.05% glutaraldehyde, and 0.5% picric acid in 0.1 M phosphate buffer (PB), pH 7.4, for 15 min. After perfusion, the brains were removed, and 100- and 350-μm-thick coronal slices were alternately cut from the left and right dorsal hippocampus.

Quantitative analysis of synapse density. For the measurement of synapse density, the 100 μm slices were treated in 1% osmium tetroxide in 0.1 mM PB, dehydrated, and then flat embedded in Durcupan resin (ACM; Fluka, Buchs, Switzerland). Corresponding small parts (0.5 × 1.0 mm) of the CA1 area in the left and right dorsal hippocampus were trimmed, and 70-nm-thick sections were collected on pioloform-coated

single-slot grids, contrasted with uranyl acetate and lead citrate, and examined with a Jeol (Tokyo, Japan) 1200EX electron microscope.

The dissector method using two adjacent (serial) sections was used to measure density of asymmetrical axospinous synapses in the CA1 area (Calverley and Jones, 1987). In the present experiment, two adjacent pairs were selected at random from serial sections of each group and were photographed without overlapping each other. Electron micrographs were obtained from the middle one-third of CA1 stratum radiatum of the dorsal hippocampus (approximately bregma −1.94 mm) (Franklin and Paxinos, 1997). The corresponding areas were photographed from the paired sections at a magnification of 15,000×. Areas of ~500 μm² were collected for each pair. Synaptic profiles on spines were identified by the presence of at least three synaptic vesicles accumulated in the presynaptic active zone, postsynaptic density (PSD), visible synaptic cleft, and rigid alignment of the presynaptic and postsynaptic membranes. Synaptic densities were evaluated according to the formula $N_V = \Sigma Q_- / V_{dis}$, where ΣQ_- represents the number of synaptic profiles present in the test section and disappeared in the corresponding area of the adjacent section. V_{dis} is the volume of the test section, obtained by multiplying the area studied by the section thickness. The area studied was measured by Scion (Frederick, MD) Image software. All analyses were performed in a blind manner.

Three mice in each experimental group and one block each from the left and right CA1 regions per animal were used. The Student's *t* test was used to determine the significance of differences ($p < 0.05$) between the mean values of data groups.

Primary antibodies. Primary antibodies used in this study were extensively characterized in previous studies and were summarized in Table 1. In the present study, we produced guinea pig polyclonal antibodies against the amino acid residues 1194–1273 of the mouse ε4 subunit (GenBank accession number D12822) and the amino acid residues 861–881 of the mouse GluR4 subunit (GenBank accession number AB022913) were generated as described previously (Fukaya and Watanabe, 2000). Using the pGEX4T-2 plasmid vector (Amersham Biosciences, Bucks, UK), the ε4 and GluR4 polypeptides were expressed as glutathione S-transferase (GST) fusion proteins and purified using the glutathione-Sepharose 4B (Amersham Biosciences). After in-column thrombin digestion, antigen polypeptides were separated from GST. The purified polypeptides were injected into female guinea pigs at intervals of 2 weeks. Antibodies for ε4 and GluR4 subunits were affinity purified using GST fusion protein-coupled cyanogen bromide-activated Sepharose 4B (Amersham Biosciences).

Immunoblot. Membrane extracts from whole brains of adult wild-type and ε4 KO mice (Ikeda et al., 1995) were prepared by homogenization in 10 vol of ice-cold buffer containing 0.32 M sucrose, 1 mM EDTA, 1 mM EGTA, 10 mM Tris-HCl, pH 7.2, and 0.4 mM phenylmethylsulfonyl fluoride, using a Potter homogenizer with 15 strokes at 800 rpm. Supernatants of the homogenates after 1000 × g centrifugation for 10 min were collected, and 50 μg per lane of protein samples were dissolved in SDS sample buffer and fractionated by 7.5% SDS-PAGE under reducing conditions. Proteins in the gel were electroblotted onto nitrocellulose membranes (BioTraceNT; Pall Gelman Laboratory, Ann Arbor, MI). The membranes were incubated with 5% skimmed milk in Tris-buffered saline containing 0.1% Tween 20 (TBST), pH 7.5 for 1 h, followed by incubation with primary antibodies (1 μg/ml) in TBST for 2 h. Immunoreaction was visualized with the ECL chemiluminescence detection system (Amersham Biosciences). As expected, GluRε4 antibody recognized a single protein band at 155 kDa in the WT but not ε4 KO, and GluR4 antibody (886–881 aa) did a single band at 99 kDa (supplemental Fig. 1, available at www.jneurosci.org as supplemental material).

For the analysis of ε2 and ζ1 in ε1 KO mice, CA1 stratum radiatum was dissected from 400-μm-thick transverse hippocampal slices prepared from 16 animals 5 d after VHC transection. Purification of PSD fraction was performed as described previously (Kawakami et al., 2003). Briefly, pooled tissues were homogenized in HEPES-buffered 0.32 M sucrose, and nuclear fraction was removed by centrifugation. Crude membrane fraction was collected by 10,000 × g centrifugation, and the pellet was layered on 0.8 M/1.0 M/1.2 M sucrose after extensive resuspension in 0.25 M sucrose. After ultra-centrifugation at 70,000 × g, 1.0 M/1.2 M sucrose inter-

Table 1. Summary of the sources, concentrations, and combinations of antibodies

Antibody against	Species (raised in)	Dilution	Primary antibodies and combinations											Secondary antibody label	Dilution	Source of primary antibody	Reference for characterization
			1	2	3	4	5	6	7	8	9	10	11				
GluRε2 (1–48 aa)	Rabbit	10 μg/ml	×	×				×						Goat anti-rabbit IgG, 5 nm gold	1:100	M. Watanabe (Hokkaido University, Sapporo, Japan)	Watanabe et al. (1998)
GluRε2 (1353–1432 aa)	Rabbit	10 μg/ml		×				×						Goat anti-rabbit IgG, 5 nm gold	1:100	M. Watanabe	Watanabe et al. (1998)
GluRζ1 (909–938 aa)	Rabbit	10 μg/ml			×									Goat anti-rabbit IgG, 5 nm gold	1:100	M. Watanabe	Yamada et al. (2001)
GluR2/3	Rabbit	5 μg/ml					×							Goat anti-rabbit IgG, 5 nm gold	1:100	AB1506 (Chemicon, Temecula, CA)	Chen et al. (1996)
GluR4 (861–881 aa)	Guinea pig	10 μg/ml				×		×						Goat anti-guinea pig IgG, 10 nm gold	1:100	M. Watanabe	Supplemental Fig. 1
GluR4 (245–273 aa)	Guinea pig	10 μg/ml				×		×						Goat anti-guinea pig IgG, 10 nm gold	1:100	M. Watanabe	Nagy et al. (2004)
		2 μg/ml							×	×				Goat anti-guinea pig, Alexa 594			
GluR4 (828–881 aa)	Rabbit	10 μg/ml				×								Goat anti-rabbit IgG, 10 nm gold	1:100	M. Watanabe	Hashimoto et al. (1999)
		2 μg/ml									×	×	×	Goat anti-rabbit, Alexa 594	1:500		
Parvalbumin	Mouse	1:1000							×					Goat anti-mouse, Alexa 488	1:500	P-3171 (Sigma, St. Louis, MO)	
mGluR1α (859–1199 aa)	Rabbit	2 μg/ml								×				Goat anti-rabbit, Alexa 488	1:500	R. Shigemoto (National Institute for Physiological Sciences, Aichi, Japan)	Shigemoto et al. (1997)
Calbindin D-28	Rabbit	1:4000									×			Goat anti-rabbit, Alexa 488	1:500	CB-38 (Swant, Bellinona, Switzerland)	
Calretinin	Rabbit	1:1000										×		Goat anti-rabbit, Alexa 488	1:500	AB 5054 (Chemicon)	Liu et al. (2003)
GluRε4 (1194–1273 aa)	Guinea pig	10 μg/ml											×	Goat anti-guinea pig, Alexa 488	1:500	M. Watanabe	Supplemental Fig. 1

× indicates inclusion of antibodies in each incubation.

face was collected and treated with 0.4% Triton X-100 for 30 min at 4°C. Triton X-100-insoluble fraction was collected as PSD fraction. Protein concentration was measured by BCA method (Pierce, Rockford, IL). Nearly the same quantities of protein were obtained from the left and right. The same amount of the protein samples were separated by SDS-PAGE and transferred to polyvinylidene difluoride membrane. The membrane was cut into two pieces at 150 kDa molecular weight and reacted with the antibodies for $\epsilon 2$ and $\zeta 1$ subunits, respectively. For enhanced chemiluminescence detection, secondary antibody conjugated with horse radish peroxidase and Western Lightning Chemiluminescence Reagent (PerkinElmer, Wellesley, MA) were used.

Postembedding immunogold labeling. For postembedding labeling, small tissue blocks of the middle CA1 area (0.5 × 1.0 mm) were trimmed from the 350-μm-thick slices of the left and right hippocampus and cryoprotected in 10, 20, and 30% glycerol in 0.1 mM PB, pH 7.4, overnight. They were then frozen by plunging into liquid propane (-185°C) in a cryofixation unit (EM CPC; Leica, Wein, Austria). Freeze substitution and low-temperature embedding in Lowicryl HM20 were performed as described previously (Matsubara et al., 1996). Briefly, the samples were immersed in 1% uranyl acetate dissolved in anhydrous methanol (-90°C, 24 h) in a cryosubstitution unit (EM AFS; Leica, Wein, Austria). The temperature was then raised (4°C/h) from -90°C to -45°C. The samples were washed three times with anhydrous methanol and infiltrated with Lowicryl HM20 resin (Polysciences, Warrington, PA) at -45°C with a progressive increase in the ratio of resin to methanol. Polymerization was performed with ultraviolet light (360 nm) at -45°C for 24 h and 0°C for 36 h. Postembedding immunogold reaction was performed as described previously (Nusser et al., 1998b). To ensure the same incubation condition, Lowicryl-embedded ultrathin sections (85 nm thickness) from both sides of CA1 were picked up onto the same grids (nickel 400 mesh). The grids were coated with coat-quick "G" medium (Daido Sangyo, Toda, Japan) to prevent detachment of the sections during processing. The sections were briefly treated with a saturated solution of NaOH in 100% ethanol for 2 s, washed, and incubated in blocking solution (2% human albumin serums in TBS with 0.1% Triton X-100) for 30 min. The sections were then incubated with the primary antibodies listed in Table 1 overnight at room temperature. After several washes with TBS for 30 min, the sections were incubated in 5 nm gold anti-rabbit IgG secondary antibody (British Biocell International, Cardiff, UK) diluted (1:100) in blocking solution containing polyethyleneglycol (molecular weight, 7500 kDa, 5 mg/ml) for 3 h. Then the sections were washed in ultrapure water, contrasted with uranyl acetate and lead citrate, and examined with a Jeol 1200EX electron microscope.

Double-labeling postembedding immunocytochemistry. Immunogold signals for $\epsilon 2$ and GluR4 subunits were visualized using 5 and 10 nm gold particles (British Biocell International), respectively. To avoid attenuation of the $\epsilon 2$ signal by interference of the two primary antibodies, labeling for $\epsilon 2$ was completed before that for GluR4.

Quantification of postembedding immunogold labeling. Electron micrographs with a final magnification of 25,000× were obtained at random from the middle one-third of stratum radiatum and stratum oriens of the CA1 region. For quantification of the $\epsilon 2$ labeling in excitatory synapses on pyramidal cells, all asymmetrical axospinous synapses with distinct PSD, synaptic cleft, and presynaptic vesicle accumulation were collected for counting immunoparticle number per unit length of PSD (particles per micrometer). For quantification of $\epsilon 2$ particles in asymmetrical synapses on interneuron dendrites, interneurons were classified into two populations. Dendritic shafts with asymmetrical synapses with at least two particles (10 nm) for GluR4 were defined as GluR4 positive, and those with no GluR4 immunogold particles in asymmetrical synapses were defined as GluR4 negative. Synapses with one particle were excluded from the analysis. Particles were counted only if their centers were projected within 30 nm from the inner leaflet of the postsynaptic membrane and within 30 nm from the lateral edge of PSD. The length of PSD was measured by Scion Image software. Blind comparisons of immunogold particle density were made between the left and right hippocampus for every experimental pair. No significant difference in average

lengths of PSD between the left and right samples was detected (in most cases), which was regarded as a prerequisite for the density comparison. The Shapiro-Wilks' W test was used for determining the normality of the distribution of particle density in each animal group. Because data failed to approximate normal distributions, the Kolmogorov–Smirnov test and Mann–Whitney U test were used to determine statistical significance of difference in distributions and median values, respectively, between the left and right hippocampus. The Student's t test was used to determine the significance of differences in averaged values of mean density ($n = 3$–4) between the left and right. A level of confidence of $p < 0.05$ was adopted for statistical significance.

Double-immunofluorescence labeling. Two WT and $\epsilon4$ KO mice (9–10 weeks) (Ikeda et al., 1995) were used for immunofluorescence labeling for GluR4, $\epsilon4$, and other chemical markers (Table 1). Under deep pentobarbital anesthesia (100 mg/kg body weight, i.p.), animals were fixed transcardially with 4% paraformaldehyde in 0.1 M sodium phosphate buffer, pH 7.2, and brains were embedded in paraffin as described previously (Fukaya and Watanabe, 2000). Paraffin sections (5 μm) through the CA1 area cut with a sliding microtome (SM2000R; Leica, Nussloch, Germany) were mounted on glass slides coated with 3-aminopropyltriethoxysilane. Sections for double labeling for GluR4 and chemical markers, including PV, metabotropic glutamate receptor (mGluR) 1α, calbindin (CB), and calretinin (CR), were blocked in 10% normal goat serum for 20 min and incubated in primary antibodies for the chemical markers overnight in room temperature. Immunoreactions were visualized by 2 h incubation with Alexa fluorescein 488-labeled anti-mouse or rabbit secondary antibodies (1:500; Molecular Probes, Eugene, OR). After acquiring images using a confocal laser-scanning microscope (Fluoview; Olympus Optical, Tokyo, Japan), the sections were further processed for the second immunoreaction for GluR4 as described previously (Fukaya and Watanabe, 2000). First, the sections were pretreated with 1 mg/ml pepsin (DakoCytomation California, Carpinteria, CA) in 0.2N HCl solution at 37°C for 8 min. The sections were then processed for the second immunoreaction with the GluR4 antibody at room temperature for overnight and Alexa 594-labeled goat anti-guinea pig secondary antibody (Molecular Probes) for 2 h. Images were acquired again from the same regions using a confocal laser-scanning microscope. The superimposed images for respective double labeling were obtained by Adobe Systems (San Jose, CA) Photoshop 6.0 software. For double labeling for GluR4 and $\epsilon4$, sections were incubated overnight with a mixture of the primary antibodies after the pepsin treatment. Immunoreactions were visualized by Alexa 594-labeled goat anti-rabbit secondary antibody (Molecular Probes) for GluR4 and fluorescein-conjugated tyramide signal amplification fluorescence detection system (NEL701; PerkinElmer) for $\epsilon4$.

Electrophysiology. Transverse hippocampal slices (450 μm thick) were cut with a vibrating microtome (VT 1000S; Leica, Nussloch, Germany) in ice-cold artificial CSF (ACSF) [in mM: 119 NaCl, 2.5 KCl, 2.5 CaCl$_2$, 1.3 MgSO$_4$, 1.0 NaH$_2$PO$_4$, 26 NaHCO$_3$, and 10 glucose (saturated with 95% O$_2$/5% CO$_2$)]. A mouse brain was fixed on an agar block, which was made by two pieces of agar slopes (with a slope of 20°) stuck together at a right angle and mounted on the cutting stage. We lowered the left rear or right rear of the brain using the agar slopes when cutting the left or right brain, respectively. Slices from a similar septotemporal level of the left and right hippocampi were used for experiments. Recordings were made in a submerged slice chamber perfused with ACSF at room temperature. Electrodes filled with 0.9% NaCl were used for extracellular recording. Synaptic responses were evoked at 0.1 Hz using a bipolar tungsten electrode. A long-term potentiation (LTP)-inducing tetanic stimulus was given at 100 Hz for 1 s at baseline stimulus strength. LTPs of the field EPSP (fEPSP) slope were expressed as a percentage of mean slope value before the tetanic stimulation. Synaptic currents were recorded from CA1 pyramidal neurons using the blind-patch technique in the whole-cell voltage-clamp mode (Axopatch 1D; Molecular Devices, Union City, CA). A high-Mg^{2+} and Ca^{2+} (4 mM of MgSO$_4$ and CaCl$_2$) ACSF was used to increase membrane stability in the presence of bicuculline. Patch electrodes
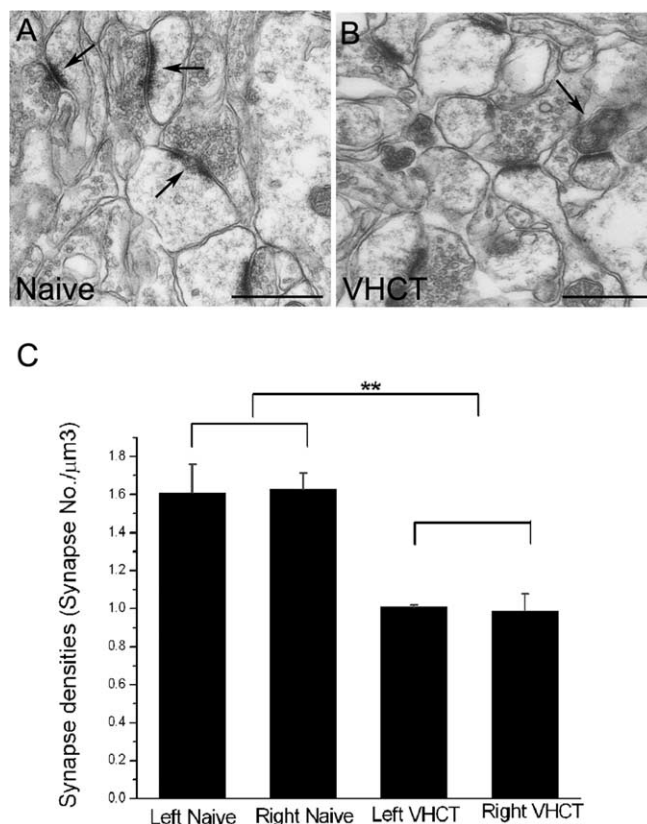
Figure 1. Reduction of synapse density after VHC transection in CA1 stratum radiatum. **A**, Axospinous asymmetrical synapses (arrows) in CA1 stratum radiatum of naive $\epsilon1$ KO mice. Scale bar, 200 nm. **B**, Corresponding area of CA1 stratum radiatum in VHCT $\epsilon1$ KO mice. Typical electron-dense type of degeneration (arrow) is occasionally observed. Scale bar, 200 nm. **C**, No significant difference ($n = 3$ animals; t test, $p > 0.05$) in density of axospinous asymmetrical synapse was detected between left (1.61 $\pm$ 0.09/μm^3) and right (1.63 $\pm$ 0.05/μm^3) stratum radiatum of the CA1 area in naive $\epsilon1$ KO mice. The mean densities decreased to 1.01 $\pm$ 0.01 and 0.99 $\pm$ 0.05/μm^3 in left and right CA1 stratum radiatum, respectively, 5 d after VHC transection (t test, **$p < 0.01$ compared with respective naive group). No significant difference ($n = 3$ animals; t test, $p > 0.05$) in synapse density was detected between left and right CA1 stratum radiatum after VHC transection.

(3–5 MΩ) were filled with an intracellular solution (in mM: 122.5 cesium gluconate, 17.5 CsCl, 10 HEPES buffer, 0.2 EGTA, 8 NaCl, 2 Mg-ATP, and 0.3 Na$_3$-GTP, pH 7.2). We recorded NMDA EPSCs at +30 mV in the presence of 6,7-dinitroquinoxaline-2,3-dione (DNQX) (20 μM) and bicuculline (30 μM). Non-NMDA EPSCs were recorded at −90 mV in the presence of bicuculline (30 μM). Series resistance (10–30 MΩ) was regularly monitored during recordings, and cells were rejected if more than a 20% change occurred during the experiment. All records were filtered at 2 kHz, digitized at 4 kHz, and stored on a computer equipped with an analog-to-digital converter (Mac Lab 2e; ADInstruments, Castle Hill, Australia). No failure was detected in our experiments. All data were expressed as a mean $\pm$ SEM and analyzed with Student's t test.

Results

Reduction of synapse density after VHC transection

To examine synapses made by ipsilateral Sch fibers selectively, synapses made by contralateral commissural fibers were eliminated by VHC transection (Kawakami et al., 2003). At 5 d after VHC transection, reactive synaptogenesis should still be very slight (Steward and Vinstant, 1983). Complete transection of VHC was confirmed in every animal operated in the present study. To confirm whether the operation successfully and evenly eliminated commissural fiber synapses in the left and right hippocampus,
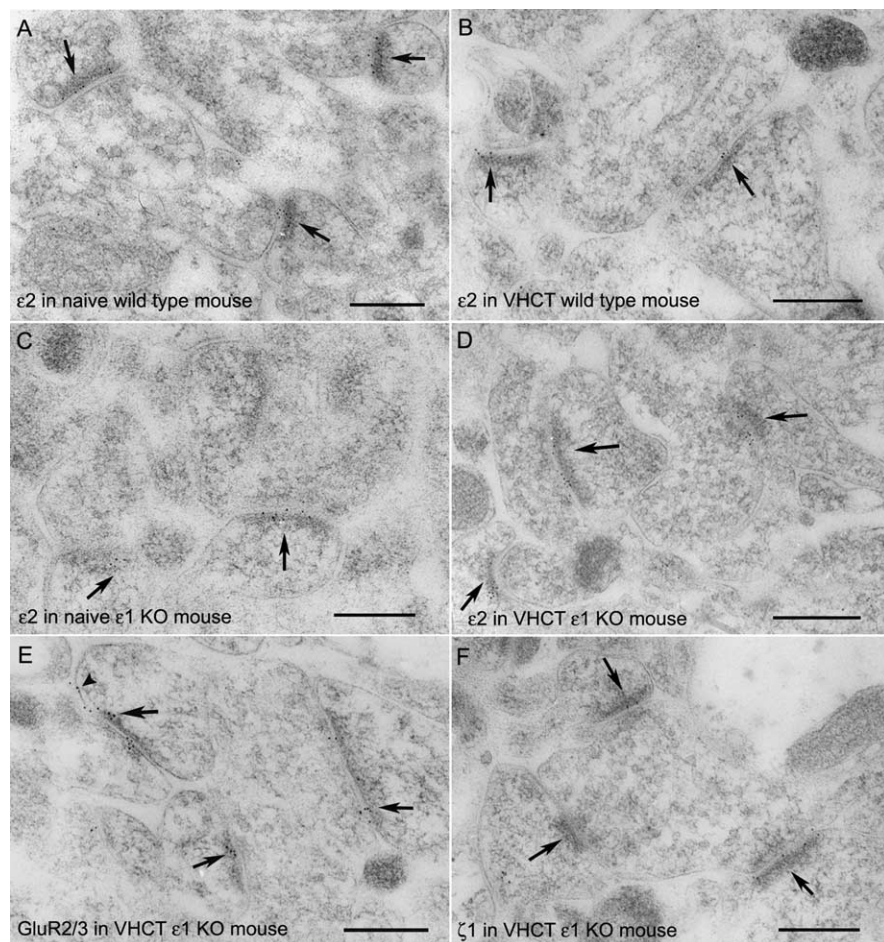
Figure 2. Postembedding immunogold labeling for $\epsilon 2$, $\zeta 1$, and GluR2/3 in pyramidal cell synapses in CA1 stratum radiatum. **A**, **B**, Immunogold labeling for $\epsilon 2$ in naive and VHCT WT mice as demonstrated with 5 nm gold particles. Immunogold particles are concentrated in asymmetrical postsynaptic membrane specialization (arrows) on pyramidal cell spines in CA1 stratum radiatum. Scale bar, 200 nm. **C**, **D**, Immunogold labeling for $\epsilon 2$ in naive and VHCT $\epsilon 1$ KO mice as demonstrated by 5 nm gold particles. Arrows indicate asymmetrical synapses on pyramidal cell spines. Scale bar, 200 nm. **E**, **F**, Immunogold labeling for GluR2/3 (**E**) and $\zeta 1$ (**F**) in VHCT $\epsilon 1$ KO mouse as demonstrated by 5 nm gold particles. Immunoparticles for GluR2/3 and $\zeta 1$ are concentrated in asymmetrical postsynaptic membrane specialization (arrows) on pyramidal cell spines in CA1 stratum radiatum. Arrowhead indicates extrasynaptic labeling. Scale bar, 200 nm.

we further examined density of intact synaptic profiles in a middle part of CA1 stratum radiatum in naive and VHC-transected (VHCT) $\epsilon 1$ KO mice. In VHCT mice (Fig. 1B) but not in naive mice (Fig. 1A), typical electron-dense-type degeneration was observed in fiber terminals. The mean density of intact axospinous asymmetrical synapses was significantly reduced ($n = 3$; Student's t test, $p < 0.05$) by 38% after VHC transection. No significant difference in synapse density was detected between left and right stratum radiatum in naive (1.61 ± 0.09 and $1.63 \pm 0.05/\mu m^3$, respectively; $n = 3$; t test, $p > 0.05$) (Fig. 1C) and VHCT (1.01 ± 0.01 and $0.99 \pm 0.05/\mu m^3$, respectively; $n = 3$; t test, $p > 0.05$) (Fig. 1C) mice. Moreover, the reduction rates were not significantly different between left and right stratum radiatum, indicating that the VHC transection denervates commissure fibers to an equivalent extent in the left and right CA1 areas.

Difference in $\epsilon 2$ labeling density between left and right Sch-CA1 pyramidal cell synapses

In naive and VHCT mice, the distribution of $\epsilon 2$ subunit in Sch-CA1 pyramidal cell synapses was compared between the left and right hippocampus by using postembedding immunogold label-

ing. Immunogold particles for $\epsilon 2$ were concentrated in type 1 (asymmetrical) axospinous postsynaptic membrane specialization (Fig. 2A–D). Most of the asymmetrical synapses on spines were immunolabeled for $\epsilon 2$ in the CA1 area (Fig. 3).

We first measured density of $\epsilon 2$ labeling in WT mice by dividing number of particles over synapses by length of the postsynaptic density. The particle density was not significantly different between left and right Sch-CA1 pyramidal cell synapses in both naive and VHCT WT mice (Mann–Whitney U test, $p > 0.05$ in all animals) (Table 2). In WT mice, despite the asymmetrical contribution of $\epsilon 2$ subunit to NMDA EPSCs, the amplitude of NMDA EPSCs relative to that of non-NMDA EPSCs was not significantly different between left and right Sch-CA1 pyramidal cell synapses (Kawakami et al., 2003). This result implies that $\epsilon 1$ subunits compensate for the difference in $\epsilon 2$ subunits in WT mice, resulting in the same NMDA receptor content in the left and right. In such a situation, postembedding immunogold labeling method may not be sensitive enough to detect difference in $\epsilon 2$ number (one or two) per NMDA receptor heteromer because of steric hindrance; two antibody molecules for $\epsilon 2$ may fail to bind two $\epsilon 2$ subunits in the same receptor channel because of the short distance between the subunits compared with the size of the antibody. Alternatively, NMDA receptors containing two $\epsilon 2$ subunits may be masked more by associating proteins than those with one subunit. Nevertheless, in $\epsilon 1$ KO mice, which have a simplified subunit composition of NMDA receptors with $\zeta 1$ and $\epsilon 2$ in CA1 pyramidal cells (Sakimura et al., 1995), the number of NMDA receptors is expected to be proportional to the amount of $\epsilon 2$ subunits. This situation could facilitate the detection of difference in the $\epsilon 2$ content with immunolabeling. Thus, we next examined distribution of $\epsilon 2$ labeling in $\epsilon 1$ KO mice.

In naive $\epsilon 1$ KO mice, the $\epsilon 2$ immunoparticle density in pyramidal cell synapses was not significantly different between left and right stratum oriens and between left and right stratum radiatum (mice 8, 9, and 10; Mann–Whitney U test, $p > 0.05$ in all animals) (Table 3). However, in VHCT $\epsilon 1$ KO mice, the density of $\epsilon 2$ immunoparticles in pyramidal cell synapses in right stratum oriens was significantly higher than that in left stratum oriens (mice 11, 12, and 13; Mann–Whitney U test, $p < 0.05$ in all animals) (Table 3). Conversely, in stratum radiatum, an opposite asymmetry was observed; the $\epsilon 2$ labeling density in the left side was significantly higher than that in the right side (mice 11, 12, and 13; Mann–Whitney U test, $p < 0.05$ in all animals) (Table 3). The averaged ratios of mean $\epsilon 2$ labeling density in the left to right were ~1:1.5 in stratum oriens and 1.44:1 in stratum radiatum ($n = 3$, respectively) (see Fig. 6). Distribution of immunoparticle density for $\epsilon 2$ in synaptic profiles was all positively

skewed toward larger value (Shapiro-Wilks' W test, $p < 0.001$) (shown for mouse 11 in Fig. 3 A, B). The distribution of $\epsilon 2$ labeling density also showed a significant difference (Kolmogorov–Smirnov test, $p < 0.05$) between the left and right with opposite directions in stratum oriens and stratum radiatum (shown for mouse 11 in Fig. 3A–D, similar results were obtained from mouse 12 and mouse 13).

Moreover, in VHCT $\epsilon 1$ KO mice, labeling density for $\epsilon 2$ was significantly different between synapses on basal and apical dendrites in stratum oriens and stratum radiatum, respectively. The density of immunoparticles for $\epsilon 2$ in basal dendrites was significantly higher than that in apical dendrites in the right hippocampus (mice 11, 12, and 13; Mann–Whitney U test, $p < 0.05$ in all animals), whereas in the left hippocampus, an opposite asymmetry was observed; the $\epsilon 2$ labeling density in apical dendrites was significantly higher than that in basal dendrites (mice 11, 12, and 13; Mann–Whitney U test, $p < 0.05$ in all animals). The averaged ratios of mean $\epsilon 2$ labeling density in the basal to apical dendrites were ~1:1.36 in the left hippocampus and 1.59:1 in the right hippocampus ($n = 3$). The $\epsilon 2$ labeling density distribution also showed a significant difference (Kolmogorov–Smirnov test, $p < 0.05$) between the basal and apical dendrites with opposite directions in the left and right hippocampus (shown for mouse 11 in Fig. 3E,F, similar results were obtained from mice 12 and 13).

As a control experiment, ultrathin sections from the same blocks were reacted with an antibody to AMPA receptor subunits GluR2/3 in CA1 stratum radiatum (Fig. 2E). Most of the spine synapses (81.6% in mouse 13) were immunopositive for GluR2/3, being consistent with previous postembedding immunogold labeling studies in the rat (Nusser et al., 1998a). In contrast to the asymmetry of $\epsilon 2$ labeling, immunoparticle density for GluR2/3 was not significantly different between left and right CA1 stratum radiatum in both naive (mice 8 and 9; Mann–Whitney U test, $p > 0.05$ in all animals) (Table 3) and VHCT $\epsilon 1$ KO mice (mice 11, 12, and 13; Mann–Whitney U test, $p > 0.05$ in all animals) (Table 3). The averaged left/right ratio of mean GluR2/3 labeling density in Sch-CA1 pyramidal cell synapses in stratum radiatum was 0.9 ± 0.1 (mean $\pm$ SD; $n = 3$) (see Fig. 6).

$\zeta 1$ subunit distribution in left and right Sch-CA1 pyramidal cell synapses
Because functional activities of the NMDA receptor channel require heteromeric assembly of $\zeta 1$ subunits with $\epsilon 2$ subunits, we
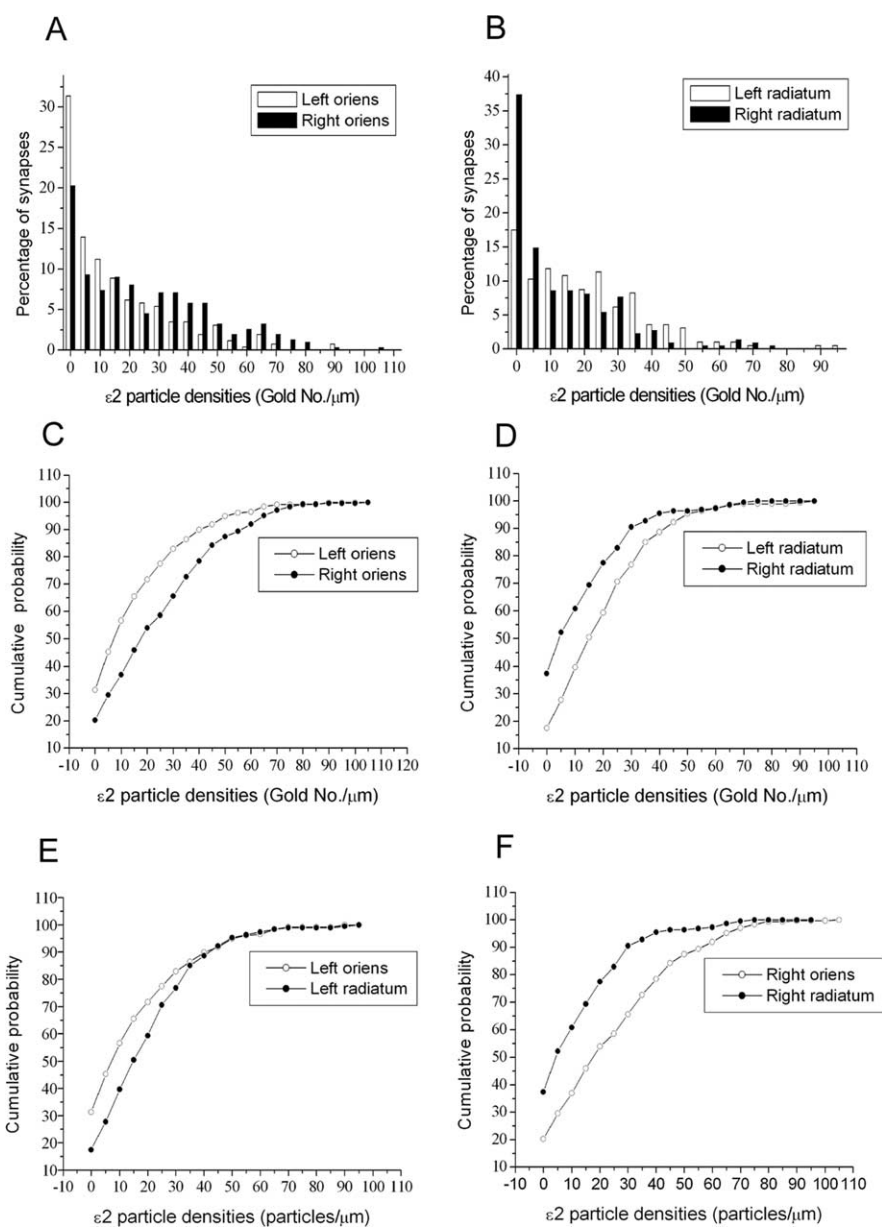

Figure 3. Mirror-image asymmetry of $\epsilon 2$ distribution in Sch-CA1 pyramidal cell synapses in $\epsilon 1$ KO mice. A, B, Histograms of $\epsilon 2$ particle density in pyramidal cell spine synapses in left and right strata oriens (A) and radiatum (B) of mouse 11. Significant difference in distribution (Kolmogorov–Smirnov test, $p < 0.05$) was detected between the left and right in strata oriens and radiatum with opposite directions. Similar results were obtained from mice 12 and 13. C, D, Cumulative probability curves of $\epsilon 2$ particle density in pyramidal cell spine synapses in strata oriens (C) and radiatum (D) of mouse 11. Mirror-image asymmetry was evident. Similar results were obtained from mice 12 and 13. E, F, Cumulative probability curves of synaptic $\epsilon 2$ density in apical (stratum radiatum) and basal (stratum oriens) dendrites of CA1 pyramidal cells in the left (E) and right (F) hippocampus of mouse 11. Significant difference in distribution (Kolmogorov–Smirnov test, $p < 0.05$) was detected between stratum oriens and stratum radiatum in the left and right hippocampus with opposite directions. Similar results were obtained from mice 12 and 13.

next compared the $\zeta 1$ distribution between left and right Sch-CA1 pyramidal cell synapses in $\epsilon 1$ KO mice.

Most of the asymmetrical spine synapses (83.2% in mouse 11) in stratum radiatum of the CA1 area were immunolabeled with an antibody to all $\zeta 1$ splice forms (Fig. 2F), being consistent with previous postembedding immunogold-labeling studies in the rat (Racca et al., 2000; Nyiri et al., 2003). In naive $\epsilon 1$ KO mice, the $\zeta 1$ immunoparticle density in Sch-CA1 pyramidal cell synapses was not significantly different between left and right stratum radiatum (mice 8 and 9; Mann–Whitney U test, $p > 0.05$) (Table 3). In VHCT $\epsilon 1$ KO mice, the $\zeta 1$ labeling density in these synapses was

Table 2. Densities of ϵ2 immunogold particles in pyramidal cell synapses of wild-type mice

Animal operation	Animal number	Stratum	Densities (particle number/μm), mean $\pm$ SD (synapse number)		Ratios (L/R)	p values (M-W test)
			Left (L)	Right (R)		
Naive	1	Oriens	11.6 $\pm$ 11.5 (206)	14.9 $\pm$ 15.4 (196)	0.78	0.11
	1	Radiatum	12.7 $\pm$ 16.7 (166)	14.0 $\pm$ 15.4 (195)	0.91	0.13
	2	Radiatum	52.4 $\pm$ 28.6 (51)	52.3 $\pm$ 28.1 (39)	1	0.94
	3	Radiatum	32.2 $\pm$ 21.9 (61)	29.0 $\pm$ 29.5 (71)	1.11	0.13
VHCT	4	Oriens	11.7 $\pm$ 12.4 (127)	14.8 $\pm$ 14.4 (106)	0.79	0.055
	5	Oriens	13.5 $\pm$ 15.2 (103)	13.7 $\pm$ 12.9 (74)	0.99	0.51
	4	Radiatum	10.5 $\pm$ 11.9 (118)	13.1 $\pm$ 14.4 (123)	0.8	0.27
	5	Radiatum	11.9 $\pm$ 12.0 (100)	11.2 $\pm$ 12.2 (104)	1.06	0.51
	6	Radiatum	31.4 $\pm$ 24.9 (57)	28.4 $\pm$ 19.3 (65)	1.1	0.67
	7	Radiatum	25.8 $\pm$ 19.2 (64)	29.9 $\pm$ 19.7 (53)	0.86	0.22

No significant difference in ϵ2 labeling density was detected between the left and right hippocampus in all animals. M-W test, Mann–Whitney U test.

Table 3. Densities of immunogold particles for NMDA and AMPA receptor subunits in pyramidal cell synapses of ϵ1 KO mice

Animal operation	Animal number	Subunits	Stratum	Densities (particle number/μm), mean $\pm$ SD (synapse number)		Ratios (L/R)	p values (M-W test)
				Left (L)	Right (R)		
Naive	8	ϵ2	Oriens	20.9 $\pm$ 19.2 (114)	15.6 $\pm$ 16.1 (90)	1.34	0.081
	9			12.7 $\pm$ 15.2 (80)	13.3 $\pm$ 14.2 (120)	0.95	0.43
	8		Radiatum	20.2 $\pm$ 16.5 (139)	21.4 $\pm$ 19.5 (169)	0.94	0.90
	9			15.8 $\pm$ 18.2 (115)	13.4 $\pm$ 15.1 (102)	1.18	0.43
	10			12.7 $\pm$ 16.3 (135)	12.3 $\pm$ 14.3 (170)	1.03	0.88
	8	ζ1	Radiatum	18.3 $\pm$ 16.7 (165)	17.0 $\pm$ 16.1 (154)	1.07	0.67
	9			9.0 $\pm$ 11.0 (149)	11.1 $\pm$ 13.0 (140)	0.81	0.16
	8	GluR2/3	Radiatum	26.3 $\pm$ 23.1 (101)	25.5 $\pm$ 21.9 (109)	1.03	0.94
	9			18.5 $\pm$ 15.8 (77)	22.7 $\pm$ 22.1 (78)	0.81	0.46
VHCT	11	ϵ2	Oriens	17.6 $\pm$ 19.3 (258)	26.8 $\pm$ 30.0 (311)	0.66	0.00*
	12			20.7 $\pm$ 20.9 (195)	29.9 $\pm$ 22.7 (201)	0.69	0.00*
	13			21.8 $\pm$ 19.8 (153)	33.3 $\pm$ 21.0 (153)	0.65	0.00*
	11		Radiatum	22.5 $\pm$ 18.1 (194)	14.5 $\pm$ 16.4 (222)	1.55	0.00*
	12			31.6 $\pm$ 23.1 (121)	20.0 $\pm$ 17.0 (129)	1.58	0.00*
	13			27.6 $\pm$ 22.1 (191)	23.3 $\pm$ 21.9 (166)	1.18	0.046*
	11	ζ1	Radiatum	26.6 $\pm$ 20.8 (120)	21.1 $\pm$ 18.7 (137)	1.26	0.033*
	12			17.9 $\pm$ 17.3 (152)	19.5 $\pm$ 17.1 (130)	0.92	0.21
	13			8.5 $\pm$ 10.6 (177)	8.8 $\pm$ 11.6 (167)	0.97	0.75
	11	GluR2/3	Radiatum	37.0 $\pm$ 27.8 (67)	41.1 $\pm$ 33.9 (65)	0.9	0.55
	12			23.8 $\pm$ 25.2 (81)	29.7 $\pm$ 25.8 (79)	0.8	0.10
	13			24.1 $\pm$ 18.4 (85)	24.7 $\pm$ 17.3 (62)	0.98	0.70

M-W test, Mann–Whitney U test. *$p < 0.05$.

also not significantly different between the left and right (mice 12 and 13; Mann–Whitney U test, $p > 0.05$) (Table 3), except one animal (mouse 11; Mann–Whitney U test, $p < 0.05$) (Table 3). The averaged left/right ratio of mean ζ1 labeling density in Sch-CA1 pyramidal cell synapses in stratum radiatum was 1.05 $\pm$ 0.2 (mean $\pm$ SD; $n = 3$) (see Fig. 6).

Identification of GluR4-positive interneurons
To further elucidate whether this asymmetrical ϵ2 distribution is dependent on types of postsynaptic cells, we investigated the ϵ2 distribution in Sch-interneuron synapses. Interneurons in the hippocampus possess a rich diversity and include multiple populations.

To identify synapses between Sch and a certain population of interneurons, we used labeling for GluR4, which is strongly expressed in PV-positive interneurons but not in pyramidal cells in the rat hippocampus (Catania et al., 1998). By double immunofluorescence, we found that GluR4-positive interneurons are immunoreactive for PV (Fig. 4A) but not for calbindin and calretinin (Fig. 4C,D). Most of the GluR4-immunopositive cell bodies were PV immunopositive (55 of 62, 88.7%), and all PV-

immunopositive interneurons were GluR4 immunopositive (55 of 55, 100%) in the CA1 area. The GluR4 immunoreactivity was also localized to radially oriented dendrites of interneurons in both strata oriens and radiatum of the CA1 area. The pyramidal cells were immunonegative for GluR4 (Fig. 4A1). The GluR4-immunopositive interneurons negative for PV seem to be mostly mGluR1α positive because 11.1% (10 of 90) of GluR4-immunopositive cell bodies were immunoreactive for mGluR1α (Fig. 4B). However, these double-labeled interneurons had dendrites mostly localized to the alveus and adjoining stratum oriens but not to the stratum radiatum in CA1, resembling O-LM cells (Ferraguti et al., 2004).

No difference in ϵ2 labeling density between left and right Sch-CA1 interneuron synapses
The density of ϵ2 labeling in synapses between Sch and dendrites of the GluR4-immunopositive and -immunonegative interneurons was investigated in CA1 stratum radiatum of VHCT ϵ1 KO mice. At the electron microscopic level, immunoparticles for ϵ2 were concentrated in asymmetrical synapses on dendritic shafts (Fig. 5B–D). Immunogold labeling for GluR4 was found less fre-

quently in asymmetrical synapses on dendritic shafts (Fig. 5A,D). However, all asymmetrical synapses were strongly GluR4 positive in a population of dendrites (Fig. 5A), indicating that these dendrites correspond to those of GluR4-positive interneurons visualized with immunofluorescence (Fig. 4). The $\epsilon2$ immunoparticle density was not significantly different between left and right Sch-CA1 interneuron synapses for both GluR4-positive and GluR4-negative interneurons (mice 11, 12, and 14; Mann–Whitney U test, $p > 0.05$ in all animals) (Table 4). The averaged left/right ratios of immunoparticle density for $\epsilon2$ in synapses on GluR4-positive and GluR4-negative interneurons were 0.88 ± 0.07 and 1.14 ± 0.2 ($n = 3$) (Fig. 6), respectively. In addition, the mean $\epsilon2$ immunoparticle density in GluR4-positive interneuron synapses was approximately four times less than that in GluR4-negative interneuron synapses and in pyramidal cell synapses.

Immunoreactivity for $\epsilon4$ in GluR4-positive interneurons

Some *in situ* hybridization studies suggested that $\zeta1$, $\epsilon1$, and $\epsilon2$ mRNAs are dominant in hippocampal pyramidal cells, whereas $\zeta1$, $\epsilon1$, $\epsilon2$, and $\epsilon4$ mRNAs are expressed in several subsets of GABAergic interneurons, including PV-positive interneurons in CA1, CA3, and dentate gyrus of adult hippocampus (Monyer et al., 1994; Standaert et al., 1996), indicating that subunit compositions of the NMDA receptor may be different between pyramidal cell and interneuron synapses. If so, NMDA receptors containing $\epsilon4$ subunit may hamper detection of asymmetrical $\epsilon2$ distribution in interneuron synapses even in $\epsilon1$ KO mice, just as $\epsilon1$ may do in WT Sch-CA1 pyramidal cell synapses. To investigate whether $\epsilon4$ is also localized to GluR4-positive synapses, we conducted double-immunofluorescence experiments (Fig. 7). Immunoreactivity for $\epsilon4$ was scattered in a punctuate manner in all layers of the CA1 area but most densely in pyramidal cell layer (Fig. 7B). Some interneuron cell bodies were also $\epsilon4$ immunopositive. These $\epsilon4$-immunopositive profiles were totally abolished in $\epsilon4$ KO mice (data not shown). We found overlap of GluR4 and $\epsilon4$ immunoreactivity in some interneuron somata (6 of 8, 75%) but not in the dendrites of GluR4-immunopositive interneurons (Fig. 7C), suggesting that $\epsilon4$ subunit is expressed in GluR4-positive interneurons but not a major component of NMDA receptors in GluR4-positive synapses.

Asymmetry of NMDA EPSCs between left and right Sch-CA1 synapses in $\epsilon1$ KO VHCT mice

To examine whether the asymmetrical $\epsilon2$ allocation actually causes differences in left–right NMDA receptor content in $\epsilon1$ KO mice, we further characterized NMDA EPSCs at CA1 pyramidal neuron synapses in slices prepared from WT and $\epsilon1$
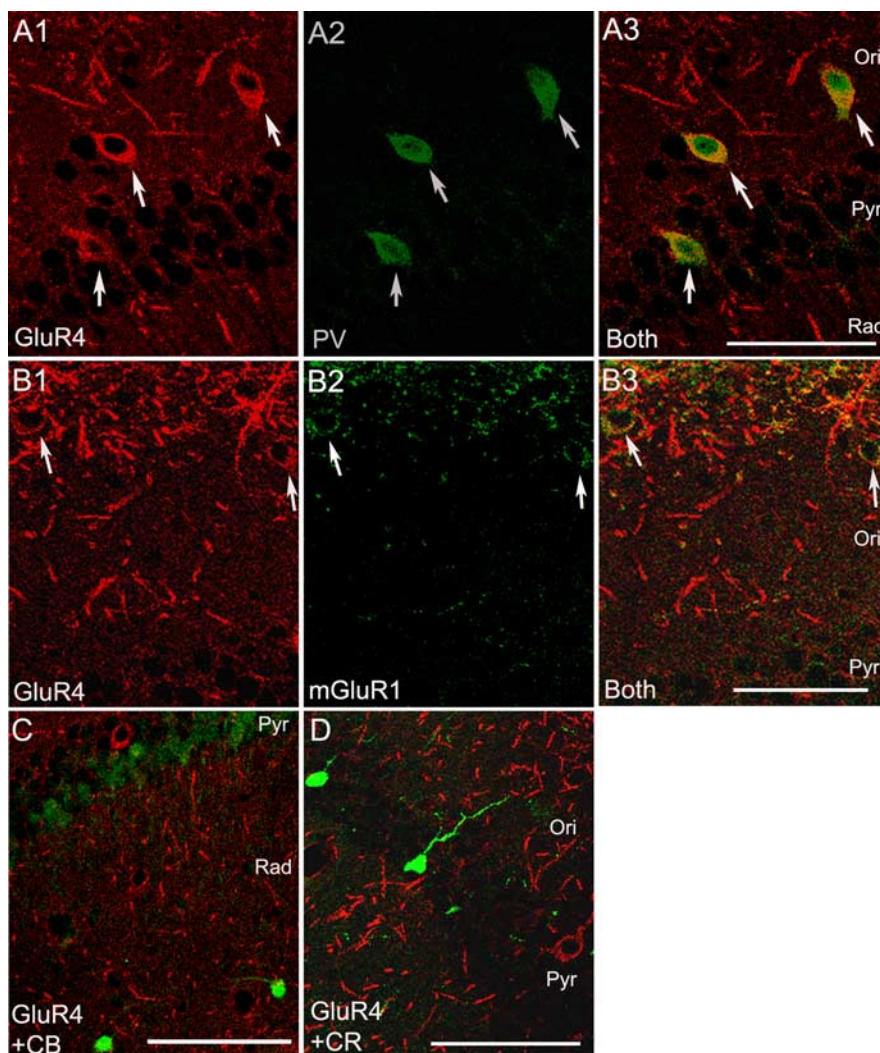

Figure 4. Colocalization of GluR4 with PV and mGluR1α in CA1 interneurons. *A*, Cell bodies of GluR4-immunopositive (*A1*) interneurons (arrows) are mainly localized in stratum pyramidale (Pyr) and adjoining stratum oriens (Ori) and mostly colabeled for PV (*A3*). All PV-positive interneurons (*A2*) are GluR4 positive. The GluR4 signal is also localized to radially oriented dendrites of interneurons in both strata oriens and radiatum (Rad). Note that the pyramidal cells are immunonegative for GluR4. *B*, Some interneuron cell bodies (arrows) in stratum oriens and alveus are labeled for GluR4 (*B1*). Cell bodies of mGluR1α-immunopositive interneurons (*B2*) are mainly found in the alveus and adjoining stratum oriens in the CA1 area, and some of them are also labeled for GluR4 (*B3*). Scale bar, 50 μm. *C*, *D*, Cell bodies of GluR4-immunopositive interneurons (red) are immunonegative for CB (*C*) and CR (*D*) shown in green. Strongly CB-immunopositive neurons are present in the distal one-third of stratum radiatum. Some superficially located pyramidal cells were also weakly positive for CB. CR-immunopositive interneurons are mainly found in stratum pyramidale. Scale bar, 50 μm.

KO VHCT mice. To record NMDA EPSCs, whole-cell patch-clamp recordings were made from CA1 pyramidal neurons in the presence of DNQX (20 μM) and bicuculline (30 μM) at a holding potential of $+30$ mV. Because excitatory synapses on CA1 pyramidal neurons localized on both apical and basal dendrites, NMDA EPSCs were independently elicited by electrical stimuli applied at either stratum oriens (basal dendritic synapses) or stratum radiatum (apical dendritic synapses) of the CA1 area.

In VHCT WT mice, stimulating the Sch fibers to CA1 stratum oriens elicited NMDA EPSCs with similar amplitude between left and right (Fig. 8A, left, middle panel, WT). The NMDA components of EPSCs evaluated by the ratio of NMDA and non-NMDA EPSCs evoked at the same stimulation intensity were indistinguishable between the left and right side slices (left basal, 57 $\pm$ 7.3%, $n = 5$ from 5 animals; right basal, 64 $\pm$ 5.7%, $n = 5$ from 5
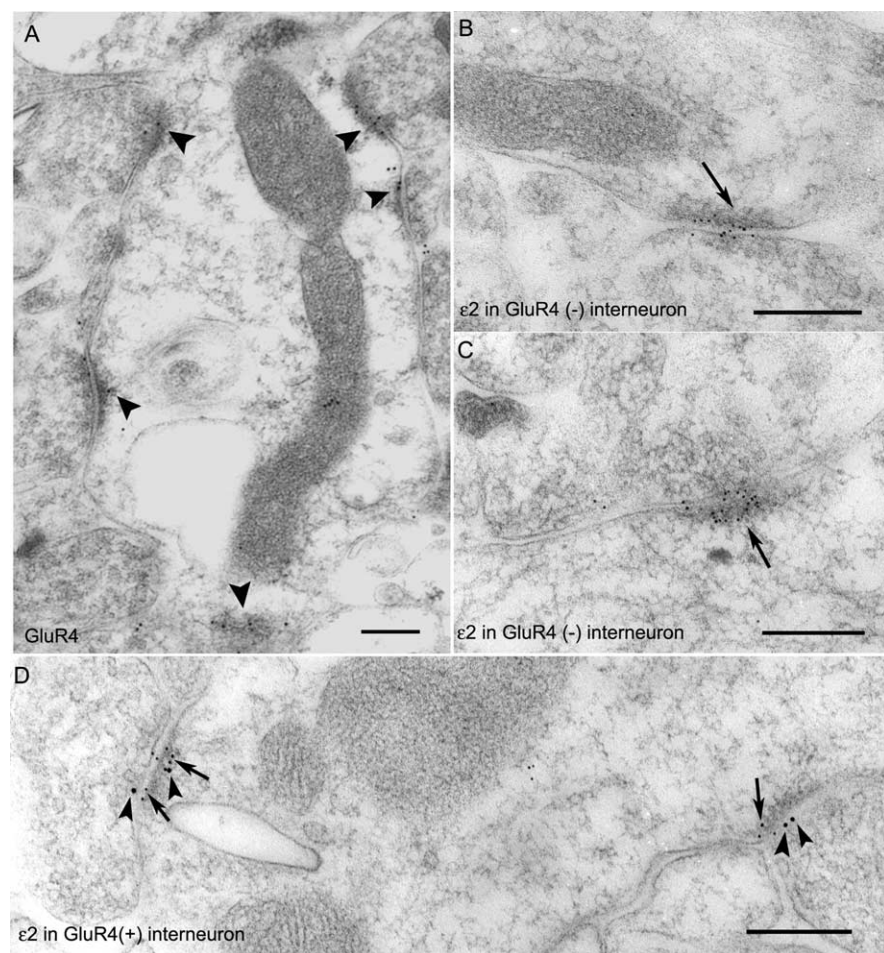
Figure 5. Postembedding immunogold labeling for ϵ2 in Sch-CA1 interneuron synapses. **A**, Immunogold particles (10 nm) for GluR4 are concentrated in type 1 (asymmetrical) synapses (arrowheads) on interneuron dendrites. Scale bar, 200 nm. **B**, **C**, Immunogold particles (5 nm) for ϵ2 are concentrated in asymmetrical synapses (arrows) on dendrites of GluR4-negative interneurons. Scale bar, 200 nm. **D**, Immunogold particles (5 nm, arrows) for ϵ2 in GluR4-immunopositive (10 nm, arrowheads) asymmetrical synapses on dendritic shafts. Immunogold particles for ϵ2 and GluR4 are mostly concentrated in postsynaptic membrane specialization. Scale bar, 200 nm.

NMDA EPSCs with similar amplitude in both sides (Fig. 8B, left, middle panel). The amplitude ratios of NMDA EPSCs to non-NMDA EPSCs, evoked at the same stimulation intensity, were indistinguishable between the left and right slices (left apical, $62 \pm 7.4\%$, $n = 5$ from 5 animals; right apical, $61 \pm 3.9\%$, $n = 5$ from 5 animals; $p > 0.05$, t test) (Fig. 8B, right, WT). In contrast, in VHCT ϵ1 KO mice, stimulating the Sch fibers to CA1 stratum radiatum elicited NMDA EPSCs with mirror-image asymmetry of that found in stratum oriens (Fig. 8B, left, bottom panel). The amplitude ratios of NMDA EPSCs to non-NMDA EPSCs were larger in the left than right hippocampal slices (left apical, $39 \pm 3.4\%$, $n = 6$ from 6 animals; right apical, $16 \pm 3.1\%$, $n = 5$ from 5 animals; $p < 0.01$, t test) (Fig. 8B, right, $\epsilon1^{-/-}$).

Asymmetry in LTP

NMDA receptors mediate associative activity-dependent changes in synaptic efficacy, including LTP in the hippocampus. Consistent with the asymmetrical content of NMDA receptors in VHCT ϵ1 KO mice, different amplitudes of LTP were found in Sch-CA1 synapses in stratum radiatum (Fig. 9). The amplitude of LTP was significantly higher in left Sch-CA1 synapses than that in the right Sch-CA1 synapses (left, $138 \pm 2.8\%$, $n = 7$ from 7 animals; right, $104 \pm 2.8\%$, $n = 6$ from 6 animals; $p < 0.05$, t test), whereas the LTP amplitudes were similar between left ($153 \pm 4.7\%$; $n = 6$ from 6 animals) and right ($150 \pm 6.3\%$; $n = 5$ from 5 animals) Sch-CA1 synapses in WT mice.

Discussion

Target-cell-specific asymmetry of ϵ2 allocation in synapses made by Sch fibers in CA1

By quantitative immunogold labeling method, we found target-cell-specific left–right asymmetry of ϵ2 allocation in synapses made by Sch fibers on CA1 pyramidal cells in ϵ1 KO mice. In the same experimental conditions, no such asymmetry was detected for ζ1 and GluR2/3 distribution in Sch-CA1 pyramidal cell synapses. The ϵ2 distribution has a mirror-image left–right asymmetry between strata oriens and radiatum, showing another asymmetry between the apical and basal dendrites. These results agree very well with the previous electrophysiological and immunoblot studies in WT mice (Kawakami et al., 2003). The opposite left–right asymmetry is expected for ϵ2 distribution in commissural fiber synapses because the difference in ϵ2 density was neutralized in naive ϵ1 KO mice and the opposite asymmetry was actually found in wild-type mice (Kawakami et al., 2003).

Expression of synaptic receptors depends on postsynaptic cell types receiving common afferents as well as on different afferent types innervating common postsynaptic cells (Shigemoto et al., 1996; Nusser et al., 1998a; Kumar and Huguenard,

animals; $p > 0.05$, t test) (Fig. 8A, right, WT). In contrast, in VHCT ϵ1 KO mice, stimulating the Sch fibers to CA1 stratum oriens elicited NMDA EPSCs with different amplitudes (Fig. 8A, left, bottom panel). The amplitude ratios of NMDA EPSCs to DNQX-sensitive non-NMDA EPSCs, evoked at the same stimulation intensity, were larger in the right than left hippocampal slices (left basal, $22 \pm 2.6\%$, $n = 5$ from 5 animals; right basal, $40 \pm 3.4\%$, $n = 5$ from 5 animals; $p < 0.01$, t test) (Fig. 8A, right, $\epsilon1^{-/-}$). Perforant path (pp) fibers from entorhinal cortex form synapses on CA1 pyramidal neurons in the stratum lacunosum moleculare (Amaral and Witter, 1995). Synaptic responses elicited by the pp-CA1 pathway were suppressed by the activation of presynaptic group II mGluRs expressed in these fibers (Petralia et al., 1996; Shigemoto et al., 1997; Kilbride et al., 1998; Contractor et al., 2000). Application of the group II selective mGluR agonist (2S,1′S,2′S)-2-(carboxycyclopropyl)-glycine (20 μM) did not depress EPSCs evoked by stimulation at CA1 stratum radiatum ($102 \pm 7\%$ of control; $n = 5$ from 5 animals), verifying that the currents were not contaminated by pp inputs.

An opposite asymmetrical effect was observed in response to stimulation at stratum radiatum (Fig. 8B). In VHCT WT mice, stimulating the Sch fibers to CA1 stratum radiatum elicited

Table 4. Density of immunogold particles for ϵ2 in pyramidal cell and interneuron synapses in stratum radiatum of VHCT ϵ1 KO mice

Animal number	Densities (particle number/μm), mean ± SD (synapse number)							p values (M-W test)					
	Pyr	GluR4(+) interneurons			GluR4(−) interneurons			Left GluR4(+) Right GluR4(+)	Left GluR4(−) Right GluR4(−)	Left GluR4(+) Left GluR4(−)	Right GluR4(+) Right GluR4(−)	Left GluR4(+) Left Pyr	Left GluR4(−) Left Pyr
	Left	Left	Right	Ratios (L/R)	Left	Right	Ratios (L/R)						
11	31.0 ± 22.4 (46)	11.9 ± 13.1 (14)	13.1 ± 12.7 (28)	0.91	36.8 ± 28.1 (39)	31.6 ± 19.6 (19)	1.16	0.80	0.35	0.002*	0.003*	0.004*	0.35
12	23.3 ± 18.3 (35)	3.4 ± 4.0 (11)	3.5 ± 5.5 (21)	0.97	17.3 ± 13.1 (14)	18.7 ± 16.1 (19)	0.93	0.82	0.76	0.015*	0.000*	0.001*	0.33
14	29.9 ± 19.7 (27)	9.5 ± 14.7 (21)	11.9 ± 13.9 (10)	0.8	26.8 ± 14.4 (19)	20.0 ± 18.0 (28)	1.34	0.44	0.095	0.001*	0.016*	0.000*	0.78

L/R, Left/Right; M-W test, Mann–Whitney U test; Pyr, pyramidal cells. *$p < 0.05$.
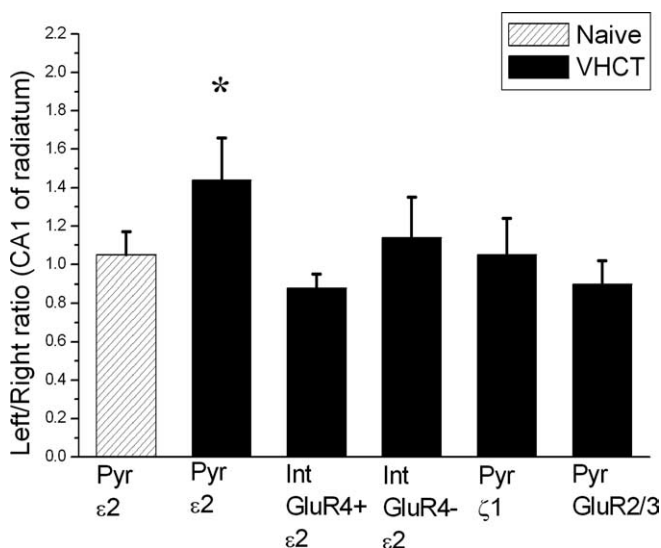
Figure 6. Summary of left/right ratios of ϵ2, ζ1, and GluR2/3 immunoparticle density in pyramidal cell and interneuron synapses in CA1 stratum radiatum of ϵ1 KO mice. Left/right ratios for ϵ2 in pyramidal cell synapses was 1.05 ± 0.12 (mean ± SD; $n = 3$) and 1.44 ± 0.22 ($n = 3$) in naive and VHCT mice, respectively. Averaged left/right ratios for ϵ2 in Sch-GluR4-positive and Sch-GluR4-negative interneuron synapses were 0.88 ± 0.07 ($n = 3$) and 1.14 ± 0.21 ($n = 3$), respectively. Those for ζ1 and GluR2/3 in Sch-pyramidal cell synapses were 1.05 ± 0.19 ($n = 3$) and 0.9 ± 0.12 ($n = 3$), respectively. A significant difference in the ratios between left and right was detected only for ϵ2 in VHCT mice (*$p < 0.05$, paired t test). Pyr, Pyramidal cells; Int, interneurons.

2003). In our previous study, we found that synaptic ϵ2 allocation in CA1 pyramidal cells is different even between the same type of afferents from left and right CA3 pyramidal cells; inputs originating in the left and right CA3 make ϵ2-dominant synapses on apical and basal dendrites, respectively, in both sides [Kawakami et al. (2003), their Fig. 4B]. In the present study, we confirmed such input-dependent asymmetry of ϵ2 allocation and further found that the target cells also influence the left–right asymmetry of receptor distribution in synapses made by common afferents (Fig. 10).

Identification of GluR4-immunopositive interneurons and ϵ2 allocation in CA1 interneuron synapses
Unlike pyramidal cells, GABAergic interneurons in the hippocampus possess a rich diversity and include multiple populations that can be distinguished on the basis of their neurochemical features (Freund and Buzsaki, 1996). In this study, we focused on two populations of interneurons in CA1 stratum radiatum, GluR4-positive and GluR4-negative interneurons, both of which had no left–right asymmetry in ϵ2 allocation.

GluR4-immunopositive interneurons and PV-immuno-positive interneurons showed a major overlap (88.7%) in CA1, being consistent with *in situ* hybridization studies suggesting dominant GluR4 mRNA expression in hippocampal PV-positive interneurons (Geiger et al., 1995; Catania et al., 1998). Dendrites of the PV-containing interneurons have a much higher synaptic coverage than other interneuron dendrites (Gulyas et al., 1999). Consistent with this observation, the GluR4-positive dendrites also had a higher synaptic coverage (Fig. 5) than the GluR4-negative ones and showed almost continuous fluorescence signals for GluR4 along dendritic arbor (Figs. 4, 7). At least three kinds of interneurons, basket cells, bistratified cells, and axo-axonic cells in the CA1 stratum pyramidale, express PV and extend their dendrites to stratum radiatum (Oliva et al., 2000; Klausberger et al., 2003, 2004), therefore, contributing to the population of GluR4-immunopositive dendrites we examined in the present study.

Previous postembedding immunogold analyses revealed that the ζ1 density in asymmetrical synapses randomly found on interneuron dendritic shafts was approximately three times as high as that on PV-positive interneuron dendrites in CA1 (Nyiri et al., 2003). Consistent with this study, we found that the ϵ2 density in asymmetrical synapses on GluR4-negative interneurons was approximately four times as high as that on dendrites of GluR4-positive interneurons, which were mostly PV positive. The low content of ϵ2 and ζ1 subunits in PV-immunoreactive neurons may cause their relative resistance to excitotoxic insults (Nitsch et al., 1989a,b).

We also found a small proportion (11.1%) of GluR4-positive interneurons expressing mGluR1α in stratum oriens. However, these neurons contribute to only a minor subpopulation of the GluR4-immunopositive dendrites we examined because their dendrites are very sparse in stratum radiatum (Ferraguti et al., 2004). The GluR4-immunonegative interneuron dendrites may at least originate from calretinin- and calbindin-containing interneurons (Fig. 4C,D), as well as from interneurons that were not identified in the present study. Although we did not detect ϵ2 density difference between left and right Sch-CA1 interneuron synapses on either GluR4-immunopositive or GluR4-immunonegative dendrites, existence of asymmetrical ϵ2 distribution in a small subpopulation of interneurons cannot be entirely excluded because the diversity of the interneurons may hamper detection of the asymmetry. Nevertheless, no clear ϵ2 asymmetry like in pyramidal cell synapses should occur in major populations of interneuron synapses in CA1 stratum radiatum.

Expression of ϵ4 in hippocampal interneurons
In situ hybridization studies suggested weak expression of ϵ4 in PV- and somatostatin-positive interneurons besides the dominant expression of ζ1, ϵ1, and ϵ2 (Monyer et al., 1994; Standaert et al., 1996). Our immunofluorescence results
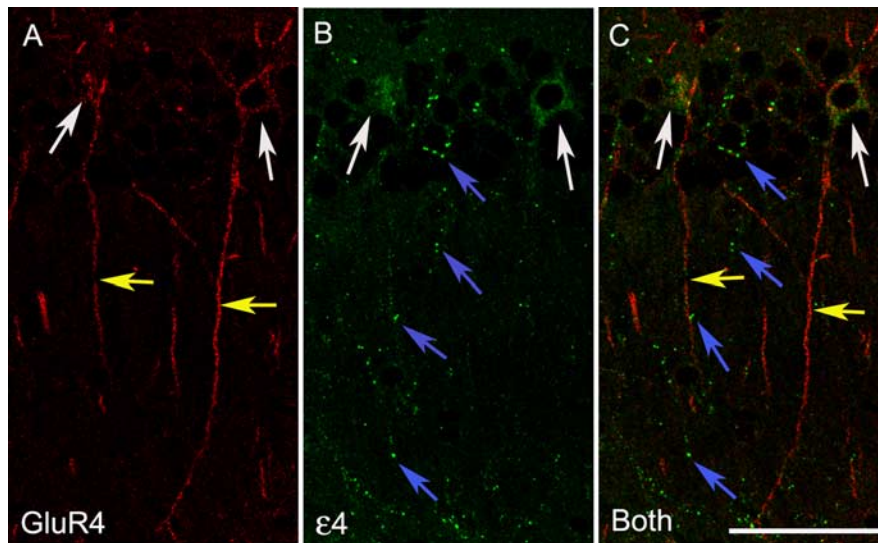
Figure 7. Different localization of ε4 and GluR4 in the hippocampal CA1 area. **A,** Cell bodies (white arrows) of interneurons and their dendrites (yellow arrows) are strongly immunolabeled for GluR4. **B,** Some cell bodies are immunopositive for ε4 (white arrows). Immunoreactivity for ε4 is also scattered in a punctate manner in strata pyramidale and radiatum (blue arrows). **C,** Overlap of immunoreactivity for GluR4 and ε4 is observed in some interneuron cell bodies but not in dendrites of GluR4-immunopositive interneurons. Scale bar, 50 μm.

showed the predominant ε4 immunoreactivity in scattered puncta and cell bodies of GluR4-immunopositive interneurons but not in the GluR4-immunopositive dendrites in CA1. Although immunogold particles for GluR4 were mostly concentrated in postsynaptic membrane specialization on the interneuron dendrites, ε4 may have a nonsynaptic localization in the GluR4-positive interneurons. NMDA receptors composed of ζ1/ε4 have distinctively slow deactivation kinetics, low single-channel conductance, and low sensitivity to voltage-dependent Mg^{2+} block (Monyer et al., 1994; Wyllie et al., 1998; Misra et al., 2000b) and are suggested to be localized to extrasynaptic membrane in several cell types in the cerebellum and hippocampus (Misra et al., 2000a,b; Brickley et al., 2003; Lozovaya et al., 2004). It is thus unlikely that ε4 composes NMDA receptors as a major subunit in the GluR4-positive interneuron synapses.

Asymmetrical NMDA receptor content between left and right Sch-pyramidal cell synapses in ε1 KO mice
In WT mice, although the amount of ε2 was different between left and right Sch-CA1 pyramidal cell synapses, the amplitude of NMDA EPSCs relative to that of non-NMDA EPSCs was the same in these synapses, indicating the same amount of NMDA receptors between left and right Sch-CA1 pyramidal cell synapses (Kawakami et al., 2003). However, in ε1 KO mice, because the NMDA subunit composition was simplified to ζ1 and ε2 in pyramidal cells (Sakimura et al., 1995), the different amount of ε2 results in different content of functional NMDA channels (Fig. 8) and distinct amplitude of LTP between the left and right hippocampus (Fig. 9). This situation is similar to that in 2-week-old WT mice (Kawakami et al., 2003), in which expression of ε1 is still very low (Watanabe et al., 1992). Based on electrophysiological and biochemical studies on subunit composition of the NMDA receptor complex (Premkumar and Auerbach, 1997; Laube et al., 1998; Hawkins et al., 1999), the functional NMDA receptor complexes in CA1 pyramidal cell synapses are assumed to consist of two or three ζ1 subunits

and two or three ε2 subunits in ε1 KO mice. Although Western blot analyses indicated that the total amount of ζ1 subunit proteins was equal between left and right Sch-CA1 synapses in WT mice (Kawakami et al., 2003), deletion of ionotropic receptor subunits could alter expression of other subunits in the heteromer at the synaptic sites (Forrest et al., 1994; Fukaya et al., 2003). Although the ζ1 expression at mRNA level had no appreciable difference in adult ε1 KO mice compared with WT mice (Sakimura et al., 1995), the present finding of functional asymmetry in NMDA receptors in Sch-CA1 synapses of ε1 KO mice raises the possibility that not only ε2 but also ζ1 subunit may have asymmetrical synaptic distribution in ε1 KO mice. However, no clear left–right asymmetry of ζ1 allocation in pyramidal cell synapses was detected (except one animal) in the present study. This may be attributable to a technical limitation in the ζ1 immunodetection or more ζ1 subunits involved in nonfunctional subunit compositions in the ε2 nondominant than ε2 dominant side of CA1. However, the former possibility is unlikely because the asymmetrical amount of ε2 but not ζ1 was also detected by immunoblot analysis (supplemental Fig. 2, available at www.jneurosci.org as supplemental material) in VHCT ε1 KO mice.

The physiological implications of left–right asymmetry of ε2 allocation
The physiological significance of the asymmetrical ε2 allocation has not yet been elucidated. The ε2 subunit plays an important role in synaptic plasticity, learning, and memory in the hippocampus (Tang et al., 1999; Clayton et al., 2002; Liu et al., 2004; Berberich et al., 2005), and left and right hippocampus could differently contribute to these behaviors (Bernasconi-Guastalla et al., 1994; Zaidel et al., 1998; Gagliardo et al., 2001). Elucidating precise allocation of the ε2 subunit is thus of fundamental importance for further understanding of hippocampal function and even the different contribution of left and right hippocampus to learning and memory. Different ε2 subunit contribution to NMDA response on the same cells was suggested depending on the side of input origin (ipsilateral or contralateral CA3 pyramidal cells) in WT mice (Kawakami et al., 2003). Considering similar and even enhanced situation in ε1 KO mice, larger contribution of NMDA receptor-mediated transmission from left than right hippocampus to stratum radiatum of both sides (Fig. 10), for example, should result in distinct information processing of inputs originated from the left and right CA3 pyramidal cells. Also, such ε2 subunit organization may provide side-dependent difference in development of synaptic strength in ε1 KO mice. The ε1 KO mice with the enhanced asymmetry in the NMDA receptor function would thus be a useful model for studying such possibilities and elucidating physiological significance of the left–right asymmetry in hippocampus-related behaviors.
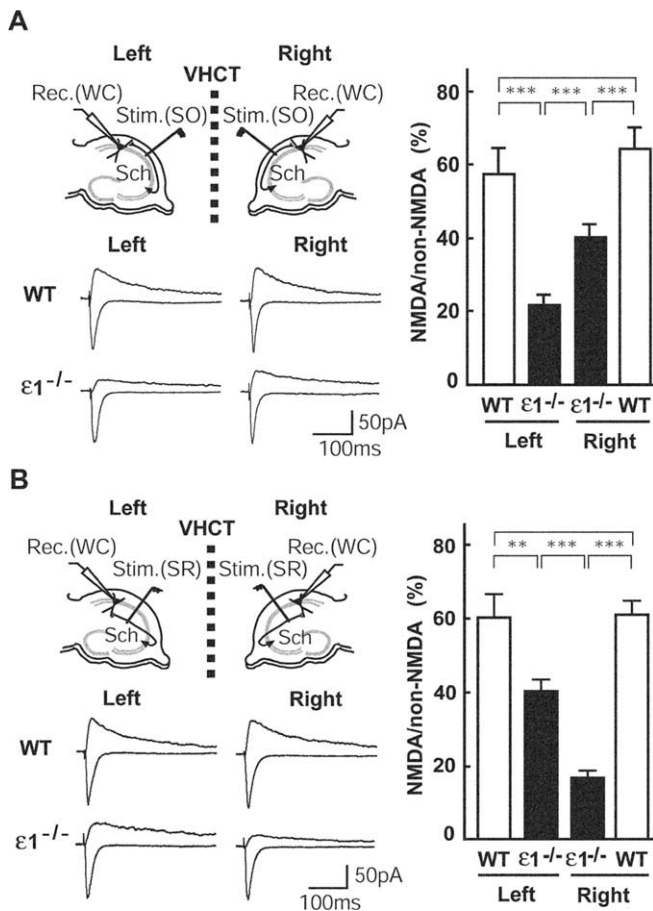
Figure 8. Left–right asymmetry of NMDA response on Sch-CA1 synapses in ε1 KO mice. **A**, Schematic diagrams showing the arrangement of electrodes for recording. To activate Sch fibers to basal dendrites of CA1 pyramidal cells, a stimulating electrode was placed in CA1 stratum oriens (SO). Whole-cell patch recordings (WC) were made from CA1 pyramidal cells. Sample superimposed traces show representative EPSCs recorded in hippocampal slices prepared from WT and ε1 KO (ε1 $^{-/-}$) mice. The top traces show NMDA EPSCs at +30 mV in the presence of DNQX and bicuculline. The bottom traces show non-NMDA EPSCs at −90 mV in the presence of bicuculline. Each trace was averaged from five consecutive recordings. Relative amplitudes of NMDA EPSCs are expressed as percentages of control responses. Columns and error bars represent means and SEM, respectively ($n = 5$ each; ***$p < 0.01$; absence of an asterisk indicates $p > 0.05$). **B**, Schematic diagrams showing the arrangement of electrodes for recording. To activate Sch fibers to apical dendrites of CA1 pyramidal cells, a stimulating electrode was placed in CA1 stratum radiatum (SR). The others were the same as those described in **A** ($n = 5$ each; **$p < 0.05$; ***$p < 0.01$; absence of an asterisk indicates $p > 0.05$). Calibration: 50 pA, 100 ms. Rec., Recording electrode; Stim., stimulating electrode.

Figure 9. Asymmetry in LTP in left and right Sch-CA1 stratum radiatum (SR) of VHCT ε1 KO mice. The top diagrams show synaptic inputs on the apical dendrites of CA1 pyramidal cells and arrangement of electrodes for extracellular recording. fEPSPs were recorded by an extracellular electrode placed in the CA1 stratum radiatum, and electrical stimuli were applied at Sch fibers of the same subfield. The middle panel shows the LTP amplitude induced in left and right Sch-CA1 stratum radiatum in VHCT WT and ε1 KO mice. Arrows indicate the time point at which a tetanic stimulation was given. Symbols and error bars represent means and SEM, respectively ($n = 5–7$). The bottom traces show representative fEPSP recorded before (1) and after (2) tetanic stimulation in the left and right VHCT WT and ε1 KO mice, respectively. Rec., Recording electrode; Stim., stimulating electrode.

Figure 10. Target-cell-specific asymmetry of NMDA receptor ε2 subunit. Left and right pyramidal neurons and their axons are colored red and blue, respectively. P, Pyramidal cells; I, interneurons; Apical, apical dendrites; Basal, basal dendrites.

References

Amaral DG, Witter MP (1995) Hippocampal formation. In: The rat nervous system (Paxinos G, ed), pp 443–494. San Diego: Academic.

Berberich S, Punnakkal P, Jensen V, Pawlak V, Seeburg PH, Hvalby O, Kohr G (2005) Lack of NMDA receptor subtype selectivity for hippocampal long-term potentiation. J Neurosci 25:6907–6910.

Bernasconi-Guastalla S, Wolfer DP, Lipp HP (1994) Hippocampal mossy fibers and swimming navigation in mice: correlations with size and left-right asymmetries. Hippocampus 4:53–63.

Brickley SG, Misra C, Mok MH, Mishina M, Cull-Candy SG (2003) NR2B and NR2D subunits coassemble in cerebellar Golgi cells to form a distinct NMDA receptor subtype restricted to extrasynaptic sites. J Neurosci 23:4958–4966.

Calverley RK, Jones DG (1987) Determination of the numerical density of perforated synapses in rat neocortex. Cell Tissue Res 248:399–407.

Catania MV, Bellomo M, Giuffrida R, Stella AM, Albanese V (1998) AMPA receptor subunits are differentially expressed in parvalbumin- and calretinin-positive neurons of the rat hippocampus. Eur J Neurosci 10:3479–3490.
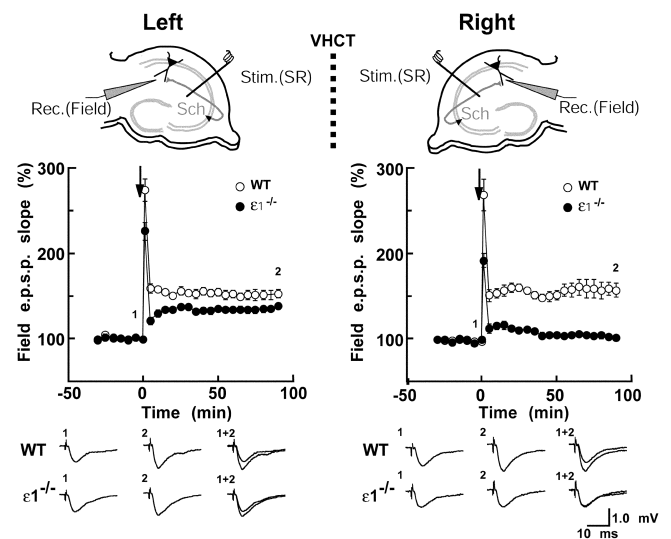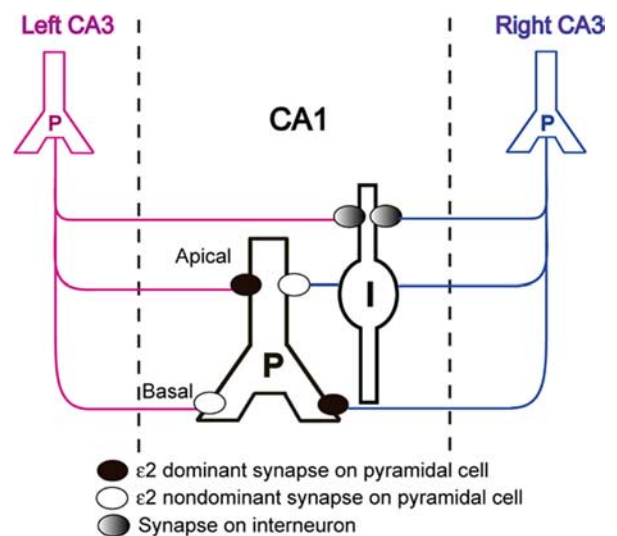
Chen Q, Veenman CL, Reiner A (1996) Cellular expression of ionotropic glutamate receptor subunits on specific striatal neuron types and its implication for striatal vulnerability in glutamate receptor-mediated excitotoxicity. Neuroscience 73:715–731.

Clayton DA, Mesches MH, Alvarez E, Bickford PC, Browning MD (2002) A hippocampal NR2B deficit can mimic age-related changes in long-term potentiation and spatial learning in the Fischer 344 rat. J Neurosci 22:3628–3637.

Contractor A, Swanson GT, Sailer A, O'Gorman S, Heinemann SF (2000) Identification of the kainate receptor subunits underlying modulation of

excitatory synaptic transmission in the CA3 region of the hippocampus. J Neurosci 20:8269–8278.

Ferraguti F, Cobden P, Pollard M, Cope D, Shigemoto R, Watanabe M, Somogyi P (2004) Immunolocalization of metabotropic glutamate receptor 1alpha (mGluR1alpha) in distinct classes of interneuron in the CA1 region of the rat hippocampus. Hippocampus 14:193–215.

Forrest D, Yuzaki M, Soares HD, Ng L, Luk DC, Sheng M, Stewart CL, Morgan JI, Connor JA, Curran T (1994) Targeted disruption of NMDA receptor 1 gene abolishes NMDA response and results in neonatal death. Neuron 13:325–338.

Franklin KBJ, Paxinos G (1997) The mouse brain in stereotaxic coordinates. San Diego: Academic.

Freund TF, Buzsaki G (1996) Interneurons of the hippocampus. Hippocampus 6:347–470.

Fritschy JM, Weinmann O, Wenzel A, Benke D (1998) Synapse-specific localization of NMDA and GABA(A) receptor subunits revealed by antigen-retrieval immunohistochemistry. J Comp Neurol 390:194–210.

Fukaya M, Watanabe M (2000) Improved immunohistochemical detection of postsynaptically located PSD-95/SAP90 protein family by protease section pretreatment: a study in the adult mouse brain. J Comp Neurol 426:572–586.

Fukaya M, Kato A, Lovett C, Tonegawa S, Watanabe M (2003) Retention of NMDA receptor NR2 subunits in the lumen of endoplasmic reticulum in targeted NR1 knockout mice. Proc Natl Acad Sci USA 100:4855–4860.

Gagliardo A, Ioale P, Odetti F, Bingman VP, Siegel JJ, Vallortigara G (2001) Hippocampus and homing in pigeons: left and right hemispheric differences in navigational map learning. Eur J Neurosci 13:1617–1624.

Geiger JR, Melcher T, Koh DS, Sakmann B, Seeburg PH, Jonas P, Monyer H (1995) Relative abundance of subunit mRNAs determines gating and Ca^{2+} permeability of AMPA receptors in principal neurons and interneurons in rat CNS. Neuron 15:193–204.

Gottmann K, Mehrle A, Gisselmann G, Hatt H (1997) Presynaptic control of subunit composition of NMDA receptors mediating synaptic plasticity. J Neurosci 17:2766–2774.

Gulyas AI, Megias M, Emri Z, Freund TF (1999) Total number and ratio of excitatory and inhibitory synapses converging onto single interneurons of different types in the CA1 area of the rat hippocampus. J Neurosci 19:10082–10097.

Hashimoto K, Fukaya M, Qiao X, Sakimura K, Watanabe M, Kano M (1999) Impairment of AMPA receptor function in cerebellar granule cells of ataxic mutant mouse stargazer. J Neurosci 19:6027–6036.

Hawkins LM, Chazot PL, Stephenson FA (1999) Biochemical evidence for the co-association of three N-methyl-D-aspartate (NMDA) R2 subunits in recombinant NMDA receptors. J Biol Chem 274:27211–27218.

Ikeda K, Araki K, Takayama T, Inoue Y, Yagi T, Aizawa S, Mishina M (1995) Reduced spontaneous activity of mice defective in the epsilon4 subunit of the NMDA receptor channel. Mol Brain Res 33:61–71.

Ishizuka N, Weber J, Amaral DG (1990) Organization of intrahippocampal projections originating from CA3 pyramidal cells in the rat. J Comp Neurol 295:580–623.

Ito I, Kawakami R, Sakimura K, Mishina M, Sugiyama H (2000) Input-specific targeting of NMDA receptor subtypes at mouse hippocampal CA3 pyramidal neuron synapses. Neuropharmacology 39:943–951.

Kawakami R, Shinohara Y, Kato Y, Sugiyama H, Shigemoto R, Ito I (2003) Asymmetrical allocation of NMDA receptor epsilon2 subunits in hippocampal circuitry. Science 300:990–994.

Kilbride J, Huang LQ, Rowan MJ, Anwyl R (1998) Presynaptic inhibitory action of the group II metabotropic glutamate receptor agonists, LY354740 and DCG-IV. Eur J Pharmacol 356:149–157.

Klausberger T, Magill PJ, Marton LF, Roberts JD, Cobden PM, Buzsaki G, Somogyi P (2003) Brain-state- and cell-type-specific firing of hippocampal interneurons in vivo. Nature 421:844–848.

Klausberger T, Marton LF, Baude A, Roberts JD, Magill PJ, Somogyi P (2004) Spike timing of dendrite-targeting bistratified cells during hippocampal network oscillations in vivo. Nat Neurosci 7:41–47.

Kumar SS, Huguenard JR (2003) Pathway-specific differences in subunit composition of synaptic NMDA receptors on pyramidal neurons in neocortex. J Neurosci 23:10074–10083.

Laube B, Kuhse J, Betz H (1998) Evidence for a tetrameric structure of recombinant NMDA receptors. J Neurosci 18:2954–2961.

Liu L, Wong TP, Pozza MF, Lingenhoehl K, Wang Y, Sheng M, Auberson YP, Wang YT (2004) Role of NMDA receptor subtypes in governing the direction of hippocampal synaptic plasticity. Science 304:1021–1024.

Liu SH, Wang J, Zhu DY, Fu YP, Lukowiak K, Lu YM (2003) Generation of functional inhibitory neurons in the adult rat hippocampus. J Neurosci 23:732–736.

Lozovaya NA, Grebenyuk SE, Tsintsadze TS, Feng B, Monaghan DT, Krishtal OA (2004) Extrasynaptic NR2B and NR2D subunits of NMDA receptors shape "superslow" afterburst EPSC in rat hippocampus. J Physiol (Lond) 558:451–463.

Matsubara A, Laake JH, Davanger S, Usami S, Ottersen OP (1996) Organization of AMPA receptor subunits at a glutamate synapse: a quantitative immunogold analysis of hair cell synapses in the rat organ of Corti. J Neurosci 16:4457–4467.

Matsuda K, Kamiya Y, Matsuda S, Yuzaki M (2002) Cloning and characterization of a novel NMDA receptor subunit NR3B: a dominant subunit that reduces calcium permeability. Mol Brain Res 100:43–52.

Misra C, Brickley SG, Farrant M, Cull-Candy SG (2000a) Identification of subunits contributing to synaptic and extrasynaptic NMDA receptors in Golgi cells of the rat cerebellum. J Physiol (Lond) 524:147–162.

Misra C, Brickley SG, Wyllie DJ, Cull-Candy SG (2000b) Slow deactivation kinetics of NMDA receptors containing NR1 and NR2D subunits in rat cerebellar Purkinje cells. J Physiol (Lond) 525:299–305.

Monyer H, Burnashev N, Laurie DJ, Sakmann B, Seeburg PH (1994) Developmental and regional expression in the rat brain and functional properties of four NMDA receptors. Neuron 12:529–540.

Nagy GG, Al-Ayyan M, Andrew D, Fukaya M, Watanabe M, and Andrew J. Todd (2004) Widespread expression of the AMPA receptor GluR2 subunit at glutamatergic synapses in the rat spinal cord and phosphorylation of GluR1 in response to noxious stimulation revealed with an antigen-unmasking method. J Neurosci 24:5766–5777.

Nakanishi S (1992) Molecular diversity of glutamate receptors and implications for brain function. Science 258:597–603.

Nitsch C, Goping G, Klatzo I (1989a) Preservation of GABAergic perikarya and boutons after transient ischemia in the gerbil hippocampal CA1 field. Brain Res 495:243–252.

Nitsch C, Scotti A, Sommacal A, Kalt G (1989b) GABAergic hippocampal neurons resistant to ischemia-induced neuronal death contain the Ca^{2+}-binding protein parvalbumin. Neurosci Lett 105:263–268.

Nusser Z, Sieghart W, Benke D, Fritschy JM, Somogyi P (1996) Differential synaptic localization of two major gamma-aminobutyric acid type A receptor alpha subunits on hippocampal pyramidal cells. Proc Natl Acad Sci USA 93:11939–11944.

Nusser Z, Lujan R, Laube G, Roberts JD, Molnar E, Somogyi P (1998a) Cell type and pathway dependence of synaptic AMPA receptor number and variability in the hippocampus. Neuron 21:545–559.

Nusser Z, Sieghart W, Somogyi P (1998b) Segregation of different GABA$_A$ receptors to synaptic and extrasynaptic membranes of cerebellar granule cells. J Neurosci 18:1693–1703.

Nyiri G, Stephenson FA, Freund TF, Somogyi P (2003) Large variability in synaptic N-methyl-D-aspartate receptor density on interneurons and a comparison with pyramidal-cell spines in the rat hippocampus. Neuroscience 119:347–363.

Oliva Jr AA, Jiang M, Lam T, Smith KL, Swann JW (2000) Novel hippocampal interneuronal subtypes identified using transgenic mice that express green fluorescent protein in GABAergic interneurons. J Neurosci 20:3354–3368.

Petralia RS, Wang YX, Niedzielski AS, Wenthold RJ (1996) The metabotropic glutamate receptors, mGluR2 and mGluR3, show unique postsynaptic, presynaptic and glial localizations. Neuroscience 71:949–976.

Premkumar LS, Auerbach A (1997) Stoichiometry of recombinant N-methyl-D-aspartate receptor channels inferred from single-channel current patterns. J Gen Physiol 110:485–502.

Racca C, Stephenson FA, Streit P, Roberts JD, Somogyi P (2000) NMDA receptor content of synapses in stratum radiatum of the hippocampal CA1 area. J Neurosci 20:2512–2522.

Sakimura K, Kutsuwada T, Ito I, Manabe T, Takayama C, Kushiya E, Yagi T, Aizawa S, Inoue Y, Sugiyama H, Mishima M (1995) Reduced hippocampal LTP and spatial learning in mice lacking NMDA receptor epsilon 1 subunit. Nature 373:151–155.

Shigemoto R, Kulik A, Roberts JD, Ohishi H, Nusser Z, Kaneko T, Somogyi P (1996) Target-cell-specific concentration of a metabotropic glutamate receptor in the presynaptic active zone. Nature 381:523–525.

Shigemoto R, Kinoshita A, Wada E, Nomura S, Ohishi H, Takada M, Flor PJ, Neki A, Abe T, Nakanishi S, Mizuno N (1997) Differential presynaptic localization of metabotropic glutamate receptor subtypes in the rat hippocampus. J Neurosci 17:7503–7522.

Standaert DG, Landwehrmeyer GB, Kerner JA, Penney Jr JB, Young AB (1996) Expression of NMDAR2D glutamate receptor subunit mRNA in neurochemically identified interneurons in the rat neostriatum, neocortex and hippocampus. Brain Res Mol Brain Res 42:89–102.

Steward O, Vinstant SL (1983) The process of reinnervation in the dentate gyrus of the adult rat: a quantitative electron microscopic analysis of terminal proliferation and reactive synaptogenesis. J Comp Neurol 214:370–386.

Sucher NJ, Akbarian S, Chi CL, Leclerc CL, Awobuluyi M, Deitcher DL, Wu MK, Yuan JP, Jones EG, Lipton SA (1995) Developmental and regional expression pattern of a novel NMDA receptor-like subunit (NMDA-L) in the rodent brain. J Neurosci 15:6509–6520.

Takumi Y, Ramirez-Leon V, Laake P, Rinvik E, Ottersen OP (1999) Different modes of expression of AMPA and NMDA receptors in hippocampal synapses. Nat Neurosci 2:618–624.

Tang YP, Shimizu E, Dube GR, Rampon C, Kerchner GA, Zhuo M, Liu GS, Tsien JZ (1999) Genetic enhancement of learning and memory in mice. Nature 401:63–69.

Watanabe M, Inoue Y, Sakimura K, Mishina M (1992) Developmental changes in distribution of NMDA receptor channel subunit mRNAs. NeuroReport 3:1138–1140.

Watanabe M, Fukaya M, Sakimura K, Manabe T, Mishina M, Inoue Y (1998) Selective scarcity of NMDA receptor channel subunits in the stratum lucidum (mossy fibre-recipient layer) of the mouse hippocampal CA3 subfield. Eur J Neurosci 10:478–487.

Wyllie DJ, Behe P, Colquhoun D (1998) Single-channel activations and concentration jumps: comparison of recombinant NR1a/NR2A and NR1a/NR2D NMDA receptors. J Physiol (Lond) 510:1–18.

Yamada K, Fukaya M, Shimizu H, Sakimura K, Watanabe M (2001) NMDA receptor subunits GluRepsilon1, GluRepsilon3 and GluRzeta1 are enriched at the mossy fibre-granule cell synapse in the adult mouse cerebellum. Eur J Neurosci 13:2025–2036.

Zaidel DW, Esiri MM, Beardsworth ED (1998) Observations on the relationship between verbal explicit and implicit memory and density of neurons in the hippocampus. Neuropsychologia 36:1049–1062.